

¹ Wind veer and speed in turbulent Ekman flow part I:
² scaling analysis and velocity profile model

³ Cedrick Ansorge¹ and Hauke Wurps^{2,3}

⁴
⁵ Submitted April 23, 2025

⁶ **Abstract**

⁷ The profiles of wind speed and direction in turbulent Ekman flow are formulated
⁸ based on asymptotic theory and data from direct numerical simulation. The profile
⁹ of the streamwise component, considered in a wall-stress-aligned reference frame,
¹⁰ follows the classical viscous, logarithmic and wake scaling. In the outer layer, the
¹¹ velocity component profiles can be described by an Ekman-spiral with adapted
¹² boundary conditions that result in a reduction of the spiral-like rotation. The
¹³ span-wise component poses a conceptual challenge to the channel-flow analogy
¹⁴ in the context of asymptotic matching; it exhibits a mixed scaling in the surface
¹⁵ layer, but follows outer scaling for most of the outer layer. Viscous stress scales
¹⁶ universally across the boundary layer in inner units while the total stress becomes
¹⁷ universal as a function of the outer height, commonly denoted as z^- . This implies
¹⁸ a mixed scaling for the turbulent stress and eddy viscosity across the inner layer
¹⁹ and convergence to a scaling as function of the outer height across the outer
²⁰ layer for increasing scale separation, i.e. for increasing Reynolds number. The
²¹ extrapolation to these scaling to atmospheric scale separation is confirmed via
²² large-eddy simulation in part II of this manuscript.

²³ **Keywords** Direct Numerical Simulation · Scale Separation · Ekman Layer · Surface
²⁴ Layer · Hodograph

²⁵ **1 Introduction**

²⁶ The Coriolis force bends the apparent path of motion on a rotating sphere and
²⁷ establishes geostrophic equilibrium when in balance with a pressure gradient force.
²⁸ Wind veer away from the wind direction in geostrophic equilibrium is (i) due to
²⁹ direct frictional effects in the very vicinity of the surface and (ii) due to turbulence

¹ FU Berlin, Institut für Meteorologie, Carl-Heinrich-Becker-Weg 6–10, 12165 Berlin, Germany
cedrick@posteo.de

² Carl von Ossietzky Universität Oldenburg, School of Mathematics and Science, Institute of Physics

³ ForWind - Center for Wind Energy Research, Küppersweg 70, 26129 Oldenburg, Germany

which exerts indirect frictional effects; these effects cause a slow-down of the mean wind reducing the Coriolis force thus turning the wind in favor of the pressure gradient force. Not only does the veering set the frame of reference for surface layer theory, it also has effects at small and large scales from large-scale dispersion via plume spreading to cyclone spin-down (Svensson and Holtslag 2009) and on the capabilities of data assimilation and accuracy of surface flux estimates (Brown et al. 2005). From a large-scale perspective, the veering of wind across the planetary boundary layer determines the amount of cross-isobaric mass-flux, commonly referred to as 'Ekman pumping' (Ekman 1905), and it is thus a key factor in the life-cycle of large-scale synoptic systems. Within the atmospheric boundary layer (ABL), directional shear of the wind in the upper part of the surface layer may cause a systematic yaw for tall wind power generation devices where blades reach into the Ekman layer, i.e. that part of the boundary layer where the wind starts to turn; an exact estimate of such effects is critical in the site assessments for wind farms (Calaf et al. 2010; Mirocha et al. 2018).

In the planetary boundary layer, wind veer is characterized by the surface veering angle α defined as the angle between the negative surface shear stress τ_{sfc} and the geostrophic wind. Surface veering α and geostrophic drag $Z \equiv u_*/G$, where the friction velocity $u_* \equiv \sqrt{|\tau_{\text{sfc}}|/\rho}$, uniquely determine the surface drag τ_{sfc} in a turbulent Ekman flow. In any quantitative description of the surface layer, the friction velocity u_* is the dynamic scale and α defines the horizontal alignment of the frame of reference, i.e. the rotation of the surface friction with respect to the outer wind direction. Knowledge about u_* and α is thus a prerequisite for any quantitative theory of the surface layer, and Rossby and Montgomery (1935) constrained the two parameters based on integral relations in the ABL. Asymptotic similarity theory was later used by Tennekes (1973); Blackadar and Tennekes (1968), and based on his seminal direct numerical simulations (DNS) of Ekman flow, Spalart (1989) suggested a modification to take into account effects of low to intermediate Reynolds numbers. Later on, constants were re-evaluated with a focus on the ABL based on observations (Högström 1988, 1996) and numerical modelling (Spalart et al. 2008, 2009; Ansorge and Mellado 2014; Ansorge 2019).

Attempts were also undertaken to obtain profiles of the wind speed: One approach is to match the inner and outer layer at a reference height as suggested by Etling (2002); Emeis (2018) (Sec. 21.10; Eq. 21.48); they choose the Prandtl-layer depth, a measure for the depth of the surface layer, to match the wind speed profiles. However, this requires external prescription of the veering at that height. A one-dimensional profile with constant veering is given by Emeis et al. (2007, Sec. 3; Eq. 3.1-3.19).

Gryning et al. (2007) present an extension of the wind-speed profile beyond the surface layer using a neutral reference profile and a stability correction; Kelly and Gryning (2010), based on a probabilistic representation of stratification, develop a model for the long-term mean wind speed in the ABL and compare this with observation at different sites; Kelly and Troen (2016) demonstrate the effect of such improved model for wind-energy applications. In consideration of the large scale separation in geophysical flow, the rotation of the wind in the surface layer is often assumed negligible, and above investigations merely focus on the wind speed; that means, the veering of the wind with height is not described and there is little knowledge on the profile of the span-wise velocity component and the precise

shape of the hodograph in the limit of a truly neutral Ekman boundary layer. A climatology of wind turning in the ABL is given by Lindvall and Svensson (2019) Klein et al. (2021) use a statistical turbulence modelling approach that yields a two-component velocity profile, but they also find that the exact representation of turning is challenging.

Ekman-layer models are roughly based on Ekman's seminal 1905 paper in combinations with additional assumptions. One option is a prescribed profile shape for eddy viscosity (Ellison (1955)), another are two-layer models of the ABL that take into account rotational effects at higher altitudes, for instance when the wind speed needs to be evaluated at heights on the order of 100 – 200 m, a particular concern when it comes to wind-power forecasting (Etling 2002; Emeis 2018; Optis et al. 2014). Despite rotational effects being considered, the formulation of these models for the outer layer and analysis of their performance primarily focuses on wind speed. Still, in 2018, Jiang et al. recognized that the outer part of the Ekman boundary layer receives less attention in comparison with the surface layer and study the neutral problem by Large-Eddy simulation (LES). They focus on the wind speed and find an extended logarithmic layer when considering the wind speed instead of the shear-aligned component, and they eventually demonstrate by means of an analytical model that this vertical extension of the logarithmic layer may be explained by a transfer of stress to the span-wise velocity component where it is assumed that the shear vector $\tau(z)$ and stress vectors $(\partial_z U, \partial_z V)$ are aligned.

More recently, Ghannam and Bou-Zeid (2021) treated the horizontally averaged momentum budget to show that departures from shear-alignment in the vicinity of the surface result in an integral of the wind veer (α_M in their notation) over the height to very high accuracy ($\int_{z_0}^H \sin \alpha_M$ in their notation; their Eq. (16)). Classic surface-layer similarity is recovered when the angle α_M does not depend on height, i.e., the wind veer is constant across the surface layer. If, however, the wind veer depends on height, the profiles of stress and mean velocities depart from the scalings implied by classic surface-layer similarity.

Turbulent Ekman flow is considered here as a conceptual model of the homogeneous, stationary ABL over a flat surface and under neutral stratification. The description of velocity profiles for this strongly simplified problem is not only a canonical fluid-mechanical problem, but it also constitutes a well-described limit for theoretical exploration or higher-order approaches taking into account possible effects of stratification, roughness or other physical complications encountered in the real geophysical system. While, on first sight, the study of such a strongly idealized case appears as an academic problem, it contains the essence of surface similarity as it is used in most atmospheric models, be it conceptual or numeric ones. More complex accounts generally refer to the homogeneous stationary problem as a base state: (i) Roughness is commonly incorporated by a linear transformation of vertical scale involving the roughness parameter z_0 and for larger roughness also a displacement height (Monin and Yaglom 1975; Jacobs and Van Boxel 1988; Högström 1988); (ii) Stability can be accounted for by a linearization around the neutrally stratified profile (Monin 1970; Monin and Yaglom 1975; Högström 1988, 1996; Sakagami et al. 2020); (iii) Non-stationarity in the pressure-gradient forcing can be accounted for by a linear damped-oscillator approach around the base state (Momen and Bou-Zeid 2016); (iv) Barotropic and baroclinic effects on the ve-

locity profile require consideration of the height-dependence of the veer and stress misalignment (Momen et al. 2018; Ghannam and Bou-Zeid 2021). Furthermore, such a solution can serve as better initial condition for numerical simulation of the flow, to minimize the length of initial transient periods, or as benchmark for turbulence closures that can be tuned to reproduce the neutral limit case.

Despite the strong simplifications implied by our choice of set-up, there is no straightforward approach to solving this well-defined problem. Large-Eddy simulation not only needs to be tuned for the surface shear stress and veering angle, but it also relies on sub-grid closures that commonly assume alignment of the turbulent stress with gradients. This pre-requisite is not fulfilled when the wind rotates with height. Esau (2004) investigated the representation of the Ekman boundary layer by dynamical subgrid closures and Zikanov et al. (2003) proposed a closure for the wind profile using a linearized representation of the eddy viscosity. Despite advances in analysis of this simplified set-up (Jiang et al. 2018), there is yet insufficient understanding for a quantitative generalization of the results to arbitrary external forcing (manifest in variation of the Reynolds number) – and indeed the fundamental questions pertaining to such relatively simple dynamics of turbulence are not reflected in the research on LES for the ABL over the past 50 years (Stoll et al. 2020).

At the same time, an increasing amount of high-quality and high-resolution data from turbulence-resolving approaches is emerging due to recent advances in high-performance computing and its application to geophysical problem sets; the geophysical range of scale separation, however, is—and it will remain so for the foreseeable future—out of reach for such simulation (Dimotakis 2005). Here, the routinely employed concept of Reynolds-number similarity can help. It postulates the existence of *fully developed turbulence* believed to occur for a sufficiently large but finite Reynolds number (Barenblatt and Goldenfeld 1995). (Already in 1998, this in fact lead Moin and Mahesh to the question *how high a Re is high enough?*) Certain statistics of fully developed turbulence, such as dissipation (Dimotakis 2005) or profiles of mean velocity (Barenblatt 1993), become independent of the Reynolds number when appropriately scaled; other statistics, such as the near-wall maximum in velocity fluctuation depend on Re (Baars and Marusic 2020) and externality of the flow may exert an impact on near-wall scaling (da Silva et al. 2014). It appears that for certain statistics in Ekman flow, fully-developed turbulence is reached with the Reynolds numbers that became possible due to an increase of computing capabilities over the past decades.

This paper exploits the robust features of mean velocity profiles from direct numerical simulation across a range of Reynolds numbers to formulate both the streamwise and span-wise components of the mean velocity vector as a function of the Reynolds number.

2 Problem formulation and numerical approach

We consider here incompressible, turbulent Ekman flow, that is, the turbulent flow over a flat rotating plate, as a physical model for the truly neutral ABL. The f-plane approximation is applied, i.e. rotation acts on the horizontal components of velocity alone; rotational effects on the vertical component of velocity and dynamical effects due to latitudinal variation of the rate of rotation are neglected.

 173 2.1 Notation and governing equations

174 The dimensional velocity vector of the numerical simulations is $\underline{U} = (U_1, U_2, U_3) =$
 175 (U, V, W) over the coordinate system $Oxyz$, where an approximate alignment (plus/
 176 minus few degrees) of the direction Ox with the surface shear stress is achieved. We
 177 consider velocity profiles only, i.e. all velocities are averaged over horizontal planes
 178 and in time, that is, they correspond to an ensemble average. The coordinate Oz
 179 points away from the wall, and Oy points in the span-wise direction normal to
 180 Oxz . For analysis of the results, we use two coordinate systems that are (i) exactly
 181 aligned with the surface shear stress

$$\underline{\tau}_{\text{sfc}} = \begin{pmatrix} \tau_x \\ \tau_y \\ \tau_z \end{pmatrix} = -\rho\nu \left(\frac{\partial U}{\partial z} \hat{e}_x + \frac{\partial V}{\partial z} \hat{e}_y \right) \quad (1a)$$

182 and labelled by an upper index α as in \underline{U}^α for the velocity vector, and (ii) the
 183 coordinate system aligned with the free-atmosphere geostrophic wind labelled by
 184 an upper index G as in \underline{U}^G . We denote the square root of the modulus of surface
 185 shear, the surface friction, by

$$u_* = \sqrt{\frac{\|\underline{\tau}_{\text{sfc}}\|}{\rho}} \quad (1b)$$

186 and let $Z_* = G/u_*$; the surface veering angle α_* is the angle between $\underline{\tau}$ and the
 187 geostrophic wind

$$\alpha_* = \sphericalangle(\underline{G}, \underline{\tau}_{\text{sfc}}). \quad (1c)$$

188 Analogously, we denote the height-local veering of the wind $\alpha(z) = \sphericalangle(\underline{G}, \underline{U}(z))$,
 189 where $\underline{G} = (G_1, G_2, 0)$ is the geostrophic wind vector.

190 We consider the incompressible Navier–Stokes equations for the three velocity
 191 components on the f-plane in a framework that is governed by (i) geostrophic wind
 192 magnitude $G = \sqrt{G_1^2 + G_2^2}$, (ii) Coriolis parameter f (representing the angular
 193 rotation), and (iii) kinematic viscosity ν . In absence of external variability, this
 194 system converges to a statistically steady state in the sense that flow statistics
 195 do not depend on time; and this state is defined by a Reynolds number, the only
 196 non-dimensional parameter that governs the system (in Ekman flow, the ratio of
 197 Rossby and Reynolds number are not independent as $Re_D = 2A_{\text{Ro}}/D$). We use
 198 the geostrophic wind as velocity and the Coriolis parameter f as time scale for the
 199 non-dimensional framework. This implies the Rossby radius $A_{\text{Ro}} = G/f$ as length
 200 scale, such that one Reynolds number governing the problem reads as

$$Re_A = \frac{GA_{\text{Ro}}}{\nu}. \quad (2)$$

201 The scales used in defining Re_A are of limited relevance for description of the
 202 turbulent flow state. The turbulence scale separation in a wall-bounded flow is
 203 commonly characterized by the friction Reynolds number (Jiménez 2012):

$$Re_\tau = \frac{u_* \delta}{\nu} = \delta^+ = \frac{Re_A}{Z_*^2}, \quad (3)$$

where $\delta = u_*/f$ and we use a superscript '+' to denote normalization by inner turbulence scales (u_*, ν) . The outer normalization (with respect to the boundary-layer depth δ and velocity u_*) is denoted by a superscript '−', i.e. $z^- = z/\delta$. Another common measure of scale separation is the Reynolds number

$$\text{Re}_D = \frac{GD}{\nu} \quad (4)$$

defined by the laminar Ekman layer thickness $D = \sqrt{2\nu/f}$.

The governing equations non-dimensionalized by G , f , and A_{Ro} read as

$$\frac{\partial u_i}{\partial t} = \frac{\partial \pi}{\partial x_i} - u_j \frac{\partial u_i}{\partial x_j} + \epsilon_{i2j}(u_j - g_j) + \frac{1}{\text{Re}_A} \frac{\partial^2 u_i}{\partial x_j^2} \quad (5a)$$

$$\frac{\partial u_j}{\partial x_j} = 0, \quad (5b)$$

where $u_i = U_i/G$ are the non-dimensional components velocity, π is non-dimensional pressure, $g_j = G_j/G$ are non-dimensionalized components geostrophic wind (with $g_1^2 + g_2^2 = 1$ by construction), and ϵ is the Levi–Civita tensor. These equations are solved inside a bounded cube of size $L_x \times L_y \times L_z$ with periodic boundary conditions in the lateral (streamwise and spanwise) directions, a no-slip–no-penetration boundary at $z = 0$, and a no-penetration, free-slip boundary at $z = L_z$.

2.2 Numerical simulations

The problem is solved numerically by tLab¹, an open-source tool-suite to simulate and analyze turbulent flows. We use here a fourth-order–five-step Runge–Kutta integration and sixth-order compact schemes for spatial derivatives in all directions. The incompressibility constraint is enforced by a fractional step approach where the Poisson equation for the pressure field is solved to machine accuracy using a combined spectral/compact approach as described in Mellado and Ansorge (2012).

Simulations used here are shown in Tab. 1. We extend an existing set of simulations for $\text{Re}_A \in \{125\,000; 281\,250; 500\,000\}$ (gray shading; cf. Ansorge and Mellado 2014, 2016) by new simulations at higher Reynolds numbers up to $\text{Re}_A = 1.28 \times 10^6$ with a horizontal domain extent up to 3.3×10^4 viscous units. In total, this yields one order of magnitude variation in terms of the scale separation in the boundary layer.

3 Scaling behavior of the flow for Re_τ up to 3000

The generalization of profiles to arbitrary Reynolds numbers requires sufficient scale separation in the simulations, not only to quantify the effect of the Reynolds number on low-order flow statistics, but also to assess the corresponding rate-of-change to eventually allow for an extrapolation of the findings. While the simulations previously available (gray shading in Tab. 1) give confidence in a first-order

¹ <https://github.com/turbulencia/tlab>

Table 1 Direct numerical simulation data sets used in this work. Re_A and Re_D refer to the Reynolds number defined in terms of the Rossby radius Λ and Ekman-layer thickness D respectively. L_{xy} is the domain size in the stream- and span-wise direction. The grid is given by the number of grid points in the stream-wise (N_x), span-wise (N_y) and vertical (N_z) directions respectively. The resolution in the span-wise and stream-wise directions are given as Δx^+ and Δy^+ . The grid in the vertical is stretched, and resolution at the wall is given by Δz^+ .

Re_A	Re_D	L_{xy}/Λ	$N_x \times N_y \times N_z$	Δx^+	Δy^+	$\Delta z^+ _{z=0}$
125 000	500	1.08	$2048 \times 2048 \times 192$	4.1	4.1	1.05
281 250	750	1.08	$3072 \times 3072 \times 384$	5.6	5.6	1.60
500 000	1 000	1.08	$3072 \times 6144 \times 512$	9.3	4.7	1.14
845 000	1 300	0.54	$2560 \times 5120 \times 640$	8.9	4.5	0.99
1 280 000	1 600	0.54	$3860 \times 7680 \times 960$	8.6	4.3	1.00

Table 2 DOIs and reference to the openly accessible data set at refubium repository

Re_D	DOI	Reference
500	10.17169/refubium-42505	Ansorge (2024a)
1000	10.17169/refubium-42507	Ansorge (2024b)
1300	10.17169/refubium-42508	Ansorge (2024c)
1600	10.17169/refubium-42509	Ansorge (2024d)

representation of the turbulent problem, the estimation of higher-order effects such as the dependency of the Reynolds number requires a broader scale separation that is made available by the two new simulations at increased Reynolds number (cf. Tab. 1). Data at such scale separation has been obtained previously (cf. Spalart et al. 2008, 2009), but we also need high confidence with respect to the convergence of simulation data for slow oscillations and with respect to sampling convergence, which translates to two further requirements on the data: First, data should be free of artifacts from long-term oscillations across the vertical extent of the domain—primarily, simulations should be free of effects originating from the inertial oscillation; this is achieved here by replacing the mean value of the three-dimensional velocity fields by the time mean over a whole inertial oscillation. Second, high accuracy is also needed in terms of the statistical convergence of averages, bulk measures and large-scale structures; this requires a domain size $L_x > \mathcal{O}(\delta_{95})$. We use here $L_x = L_y = 1.08\Lambda$ for cases with $Re \leq 1000$ and $L_x = L_y = 0.54\Lambda$ for $Re \geq 1300$ which corresponds to $L_x/\delta_{95} \approx 25$ for $Re_D = 500$ and $L_x/\delta_{95} \approx 18$ for $Re_D = 1300$.

Bulk parameters of the simulations are given in Tab. 3. The surface stress is characterized by u_* and α_* in relation to the geostrophic wind vector and discussed in more detail as the drag law below in Sec. 4.1 (we find the expected slight decrease of u_*/G and α_* with increasing Re). The boundary-layer height estimated from the 95% stress reduction, δ_{95} , is around 0.6δ to 0.66δ . Interestingly, the integrated TKE $\int_0^\delta edz$ stays constant when normalized by the friction velocity u_* while the integrated dissipation $\int_0^\delta edz$ exhibits inviscid scaling when normalized by the magnitude G of the geostrophic wind. (TKE and dissipation normalized as $fG^{-3} \int edz$ and $u_*^{-3} \int edz$, exhibit substantial dependence on Re for the variation of u_* .) This indicates that the bulk dissipation is governed by the forcing G -irrespective of Re . Changes in Re , however, affect the level and organization of turbulence, and the parameter representing this dependency is the friction veloc-

Table 3 Bulk characterization of the simulations for different Reynolds numbers Viscous Reynolds number Re , friction Reynolds number Re_τ , friction velocity u_* , surface veering angle α_* , normalized boundary layer depth δ_{95}/δ , inner normalization of vertically integrated TKE, outer normalization of vertically integrated dissipation.

Re	$\delta^+ = \text{Re}_\tau$	u_*/G	α_*	δ_{95}/δ	$f u_*^{-3} \int_0^\delta \epsilon dz$	$G^{-3} \int_0^\delta \epsilon dz$
500	479	0.0619	25.5	0.66	0.88	1.31
750	886	0.0561	21.0	0.65	0.90	1.34
1000	1403	0.0530	18.8	0.62	0.92	1.30
1300	2122	0.0501	17.9	0.59	0.85	1.24
1600	2978	0.0482	17.2	0.61	0.91	1.21

ity u_* which describes the turbulence production processes in the surface layer, in particular in the buffer layer.

Velocity profiles in inner units ($U^{\alpha+}(z^+)$, Fig. 1a) and outer units ($U^{\alpha-}(z^-)$, Fig. 1b) are in accordance with previous work (Coleman et al. 1992; Spalart et al. 2008, 2009; Ansorge and Mellado 2014; Ansorge 2019): The profiles of the shear-aligned streamwise velocity component are well-collapsed for $\text{Re}_D > 500$ below $z^- \approx 0.15$ (circles in Fig. 1a); the case with $\text{Re}_D = 500$ is only transitionally turbulent and there is no distinct inner-outer scale separation. The logarithmic law is appropriate for $50 < z^+ < 0.15\text{Re}_\tau$, where $z^+ = \text{Re}_\tau z^-$. While the profiles $U^{\alpha+}(z^+)$ diverge between different Re beyond $z^- = 0.15$, the corresponding profiles of the velocity deficit ($U^{\alpha+}(z^-) - G_1^\alpha$) agree closely, irrespective of Re . This illustrates the inner–outer scale-duality in this external flow with inner scaling being appropriate in the inner layer and outer scaling in the outer layer. Also in the outer layer of the flow, u_* (and not the magnitude of the geostrophic wind G) governs the inviscid normalization, i.e. a scaling independent of the Reynolds-number.

No collapse is found for the profiles of spanwise velocity when considered in inner units, $V^{\alpha+}(z^+)$. When normalized in outer units, the deficit profiles of spanwise velocity ($V^{\alpha+}(z^-) - G_2^\alpha$) agree well beyond $z^- \approx 0.3$. This is a much higher level in comparison with the streamwise component that collapses also within the overlap layer, i.e. much closer to the surface (circles in Fig. 1b). The value of $V^{\alpha+}(z^-) - G_2^\alpha$ is sensitive to the wind veering for $z \rightarrow 0$ as—for use of the shear-aligned component—it has to approach the value $-G_2^\alpha = |G| \sin \alpha \neq 0$ in view of the no-slip boundary condition. While low-Re effects appear to be present for $\mathcal{O}(\text{Re}) < 10^3$, the spanwise component converges to an Re -independent limit within the range of scale separation considered here, i.e.

$$G_2^\alpha/u_* = Z_* \sin \alpha \rightarrow \text{const. for } \text{Re} \rightarrow \infty, \quad (6)$$

which has indeed already been found by Spalart (1989), who estimates the constant from an integral relation.

The viscous stress

$$S_{\text{visc}} = \nu \sqrt{\left(\frac{\partial U}{\partial z} \right)^2 + \left(\frac{\partial V}{\partial z} \right)^2} \quad (7a)$$

exhibits universal scaling when considered as $S_{\text{visc}}^+(z^+)$ (Fig. 2a); this normalization is also appropriate in the outer layer where the viscous stress is, however,

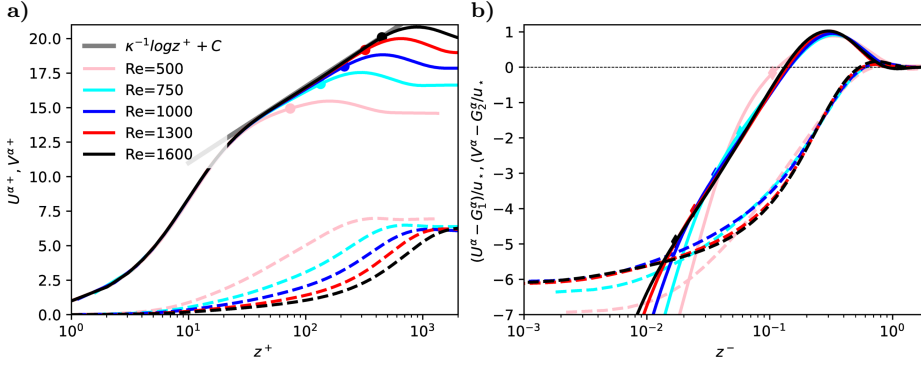


Fig. 1 a) Shear-aligned velocity profiles in inner units; circles mark the height $z^- = 0.15$; b) Shear-aligned velocity deficit in outer units; diamonds mark the grid point closest to the height $z^+ = 50$

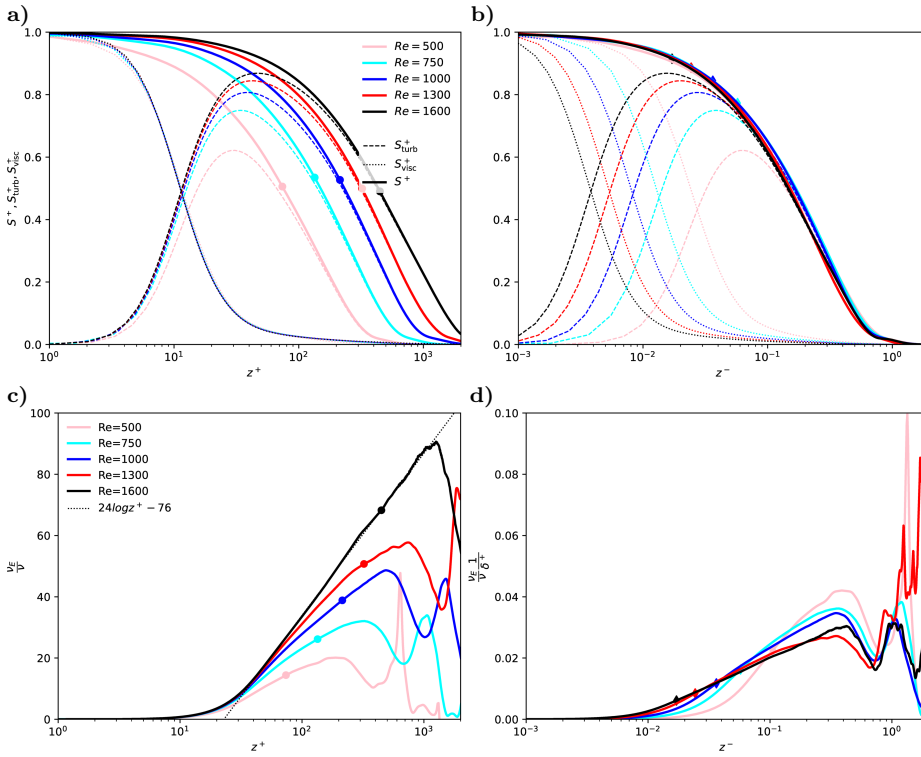


Fig. 2 a-b) Profiles of the turbulent stress S_{turb}^+ (dashed), the viscous stress S_{visc}^+ (dotted), and the total stress, $S^+ = S_{\text{visc}}^+ + S_{\text{turb}}^+$ (solid) as a function of inner height (a) and outer height (b). c-d) Normalized eddy viscosity ν_E (solid) plotted versus inner height (c) and outer height (d). (c) uses inner normalization; (d) uses normalization by $\nu \delta^+$ which approximately collapses data in the outer layer. Different colors are for different Reynolds numbers (cf. Tab. 1). Circles in (a) and (c) denote the height $z^- = 0.15$, diamonds in (b) and (d) are for $z^+ = 50$ as in Fig. 1

295 small. Small deviations from the universal profile are observed for the smallest
 296 Reynolds number $\text{Re} = 500$; we attribute these to low-Re effects in the only trans-
 297 transitionally turbulent flow ($\text{Re}_\tau = 479$). In contrast to the viscous stress, the total
 298 stress follows outer normalization, i.e. $S^+(z^-)$ is universal; a discrepancy in the
 299 inner layer does not occur as the total stress is approximately constant in the
 300 viscous and buffer layer, and a rescaling of the height would have no effect there;
 301 above, outer scaling is appropriate for the well-established dynamics in the over-
 302 lap region of inner and outer layer. This, however, implies a mixed scaling for the
 303 turbulent stress,

$$S_{\text{turb}} = \sqrt{\overline{u'w'}^2 + \overline{v'w'}^2}, \quad (7b)$$

304 where dashed quantities u' , v' , w' indicate deviations from the mean and the
 305 overbar denotes horizontal and time averaging. Indeed, S_{turb} only follows inner
 306 normalization below $z^+ \lesssim 20$ (where the turbulent contribution is negligible). In
 307 the outer layer, where $S_{\text{visc}} \rightarrow 0$, S_{turb}^+ follows outer normalization for $z^- \gtrsim 0.15$ —
 308 with increasing accuracy for larger Re and larger distance from the surface. In the
 309 overlap region, i.e. for $z^+ > 20$ and $z^- < 0.15$, the mixed scaling for the turbulent
 310 stress can be expressed as

$$S_{\text{turb}}^+(z^+, \text{Re}_\tau) = S^+(z^-) - S_{\text{visc}}^+(z^+), \quad (7c)$$

311 where $z^- = z^+/\text{Re}_\tau$.

312 The eddy viscosity plays a crucial part when modelling profiles and the vertical
 313 transport in turbulent flow. In analogy to the Fick-law for molecular diffusion,
 314 the eddy diffusivity is the effective diffusivity that yields the turbulent transport
 315 S_{turb} based on the strain rate. For the assumptions of horizontal homogeneity and
 316 incompressibility (which implies $W = 0$, i.e. no mean wall-normal velocity), it is

$$\nu_E = \frac{S_{\text{turb}}}{\sqrt{\left(\frac{\partial U}{\partial z}\right)^2 + \left(\frac{\partial V}{\partial z}\right)^2}} = \nu \frac{S_{\text{turb}}}{S_{\text{visc}}}. \quad (8a)$$

317 The inner normalization of ν_E is obtained when dividing by the molecular viscosity:

$$\nu_E^+ = \nu_E/\nu = S_{\text{turb}}/S_{\text{visc}}. \quad (8b)$$

318 Under this normalization, the profiles of eddy viscosity collapse below $z^+ \approx 20$
 319 with a tendency towards better collapse at higher z^+ for higher Reynolds number
 320 (up to $z^+ \approx 50$ for $\text{Re} = 1600$; Fig. 2c). In the outer layer, the eddy viscosity
 321 is characterized by a distinct minimum at $z^- \approx 0.6 - 0.8$, and we find that the
 322 following mixed normalization of ν_E by the geostrophic wind and friction velocity
 323 collapses the value of ν_E at this minimum (cf. Fig. 2d):

$$\nu_E^- = \nu_E^+ \frac{1}{\delta^+} = \nu_E \frac{1}{\nu} \frac{\nu}{u_* \delta} = \nu_E \frac{f}{u_*^2}. \quad (8c)$$

324 Substantial variation of the profiles is, however observed below and above this
 325 minimum for different Re which illustrates that this normalization is probably not
 326 generally appropriate across the outer layer.

327 The organization of the flow with $\text{Re}_\tau = 2978$ is depicted in terms of the
 328 turbulence kinetic energy in Fig. 3. In vicinity of the wall, at $y^+ \approx 10$, (Fig. 3a),
 329 elongated streaks aligned with the surface shear stress dominate. Moving away

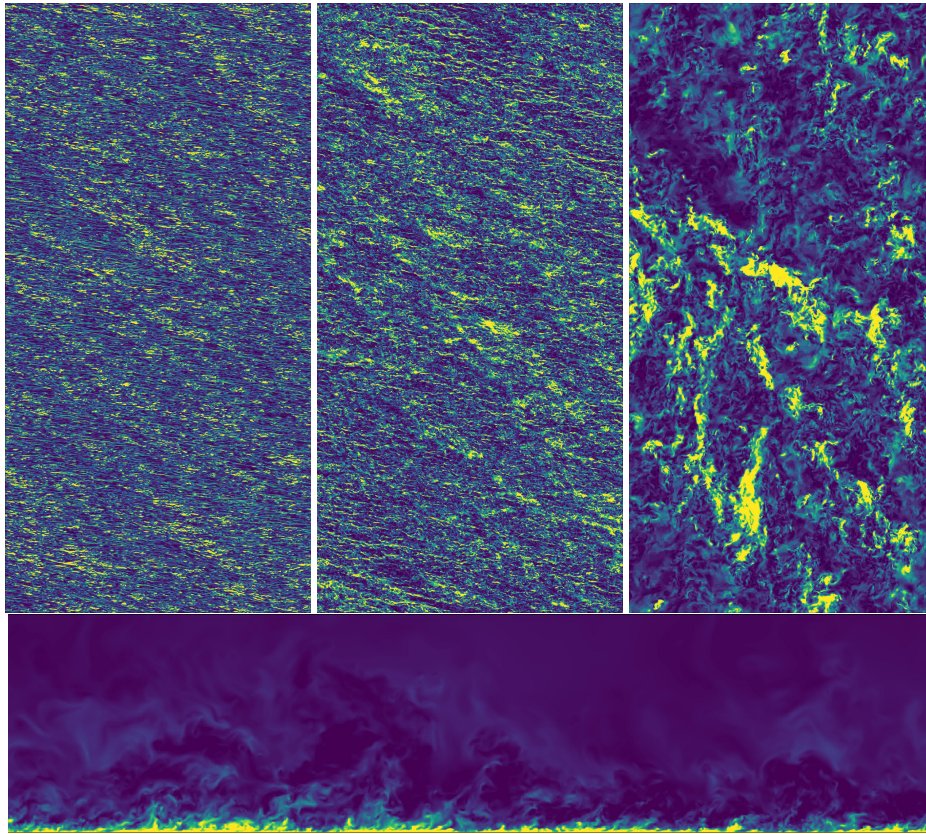


Fig. 3 Horizontal slices of turbulence kinetic energy in the Buffer layer ($i=10, z^+ \approx 10.5$), logarithmic layer ($i=100, z^+ \approx 150$), and outer layer ($i=400, z^+ \approx 1200$) of the case with $Re_\tau = 2978$; coloring between percentiles 4 and 96 of the respective image. Lower panel: streamwise–vertical intersect through the domain

330 from the wall, to $y^+ \approx 150$ (well within the logarithmic region), the structures are
 331 larger and more isotropic, but they are still largely aligned with the surface shear
 332 stress. In the upper part of the outer layer, around $y^+ \approx 1000$, no clear signature of
 333 the surface veering direction is found, and intense TKE structures (bright yellow)
 334 are organized on a large spatial scale with weaker eddies (greenish structures) and
 335 quiescent regions in between.

336 **4 A Reynolds-number-independent velocity profile for the turbulent
 337 Ekman layer**

338 We now turn to the formulation of a general velocity profile that is fully determined
 339 by the only parameter of the idealized problem, namely a Reynolds number repre-
 340 senting the scale separation or geometric size of the problem. This precludes, first,
 341 a drag law wherewith we begin this section (4.1). Based on the scaling arguments
 342 put forward in Sec. 3, we then develop, second, a formulation of the wind vector

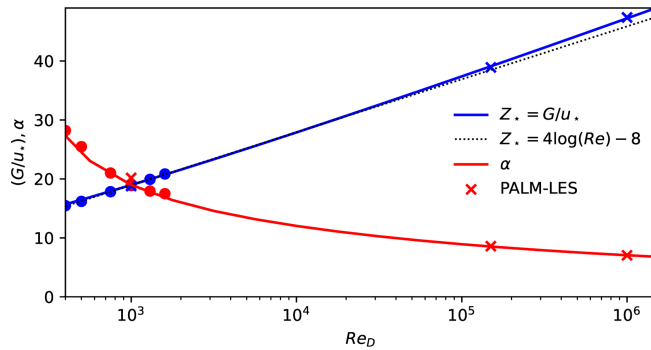


Fig. 4 Variation of geostrophic drag, Z_* , and surface veering, α_* , with Reynolds number according to the theory by Spalart et al. (1989) and as estimated from DNS data

343 in the Ekman layer (Sec 4.2). Finally, we come up with a separate formulation of
 344 the, third, stream-wise and, fourth, span-wise velocity components in the overlap
 345 and inner regions of the flow.

346 4.1 Drag-law

347 A drag-law for Ekman flow determines—as a function of Reynolds number alone—
 348 the surface drag. This can be formulated by the normalized surface friction, u_*
 349 (Eq. (1b), also termed geostrophic drag), and the direction of surface shear stress,
 350 α_* (Eq. (1c), also termed wind veer). A non-zero veering of the wind is a rather
 351 special case in comparison with most turbulent flows considered in an engineering
 352 context, and it confronts us with a situation where the most appropriate coordinate
 353 system for analysis (namely that aligned with the surface shear stress) is a priori
 354 unknown. We compare our DNS data against a semi-empirical drag-law based on
 355 integral consideration (Spalart 1989) and find, as demonstrated in previous work
 356 (Ansorge and Mellado 2014), excellent agreement in the range $400 < \text{Re} < 1600$,
 357 representing a factor of 16 in variation of viscosity.

358 We also find that the solution of the transient equation involved in estimation
 359 of u_* for a given Reynolds number Re_D is approximated reasonably by the
 360 formulation

$$Z_* = 4 \log(\text{Re}_D) - 8 \quad (9)$$

361 which quantifies the 'weak' dependence of u_* on the Reynolds number as an ap-
 362 proximately logarithmic one, at least for problems with a scale separation on the
 363 order that is relevant to geophysical problems ($Re_D < 10^8$).

364 4.2 Profile in the Ekman layer

365 Formulations for the outer layer that take into account the rotation (and thus
 366 deviation from the channel-flow analogy) need to be matched to the framework of
 367 surface similarity. A smooth transition from the inner layer to the Ekman layer,
 368 where the wind is characterized by a turning of its mean direction, is not eas-
 369 ily achieved. Optis et al. (2014), for instance, define an “*effective geostrophic wind*

370 vector that has the same magnitude of the observed surface geostrophic wind and is rotated
 371 by the angle α [their nomenclature]” to overcome the unsteady transition when
 372 approaching the Ekman layer from below. Such rotation of the wind vector is *a posteriori*
 373 justified by the observational data that the model outcomes are compared to. This need for a connection of the two reference frames is a manifestation
 374 of a mismatch in the theoretical treatment of the inner and outer layer in this
 375 rotating flow configuration.

377 The text-book solution for Ekman flow makes use of the physical boundary
 378 conditions (BCs) for the ABL (no-slip at the bottom and geostrophic wind in the
 379 free atmosphere) and a constant eddy viscosity. Specifying the boundary conditions
 380 at top and bottom eliminates one mode of the analytical solution, and it determines
 381 the magnitude of the spiral. In doing so, one has to assume that the solution is
 382 appropriate across the entire ABL, which is not the case: The dynamics put forth
 383 by Ekman in 1905 are not appropriate in the surface layer of the ABL; better
 384 approximations exist for the logarithmic, buffer, and viscous sublayers. In view of
 385 this situation, we use an adapted Ekman spiral that does not enforce the boundary
 386 conditions at the surface but at a different height while maintaining the restriction
 387 to constant eddy viscosity. This is achieved by considering the Ekman spiral only in
 388 the Ekman layer, thus giving way for the well-established logarithmic and viscous-
 389 layer profiles in the lower surface layer. Based on the derivation in App. A.1, this
 390 profile is given by

$$\frac{1}{G} \begin{pmatrix} U_{ek} \\ V_{ek} \end{pmatrix} = \begin{pmatrix} 1 \\ 0 \end{pmatrix} + e^{-z_{ek}} \left[a_{ek} \begin{pmatrix} -\cos z_{ek} \\ \sin z_{ek} \end{pmatrix} + b_{ek} \begin{pmatrix} \sin z_{ek} \\ \cos z_{ek} \end{pmatrix} \right]. \quad (10a)$$

391 with $z_{ek} = \delta_{ek}(z^- - s_{ek})$. The right-hand-side consists of two modes with magnitude
 392 a_{ek} and b_{ek} shifted by $\pi/2$ with respect to each other. In the classic case, the second
 393 mode governed by b_{ek} is incompatible with the surface boundary condition. While
 394 this is not the case here for the general form of the profile, the phase shifts can also
 395 be captured by the parameter s_{ek} , and we stick with to a single-modal approach,
 396 i.e., we let $b_{ek} = 0$.

397 This single-modal solution is characterized by three parameters, (i) an Ekman-
 398 layer depth scale δ_{ek} , (ii) the magnitude parameter of the spiral a_{ek} , and (iii) a
 399 zero-crossing point for the velocity s_{ek} . The effects of varying these parameters
 400 are illustrated in Fig. 5 where the classic Ekman solution is recovered by setting
 401 $a_{ek} = 1$, $s_{ek} = 0$ and $\delta_{ek} = \sqrt{2\nu/f}$. These parameters are *a priori* unknown as
 402 they need to conform to the turbulent state of the boundary layer; we use our
 403 DNS data to arrive at best estimates for them.

404 **The Ekman-layer depth scale δ_{ek}** is fundamentally defined by the eddy vis-
 405 cosity. However, we have seen in Section 3 that a characteristic value for the
 406 eddy diffusivity is not easily obtained for its strong dependence on the Reynolds
 407 number and distance from the surface. We therefore resort to the physical man-
 408 ifestation of the eddy diffusivity in an Ekman layer, and use the boundary layer
 409 depth $\delta_{ek} = 0.66\delta \times 2\pi$. For the relation $\delta_{ek} = \sqrt{2\nu_{ek}/f}$, this yields $\nu_{ek} \propto u_*^2/f$ in
 410 accordance with the observations in Sec. 3 (Eq. 8c).

411 **The magnitude parameter of the Ekman spiral**, a_{ek} , defines the super-
 412 geostrophic maximum of the wind profile aloft the logarithmic layer. Our simu-
 413 lations suggest this maximum of the velocity deficit remains constant when nor-
 414 malized by u_* as shown in Fig. 6. The numerical value of a_{ek} is estimated from

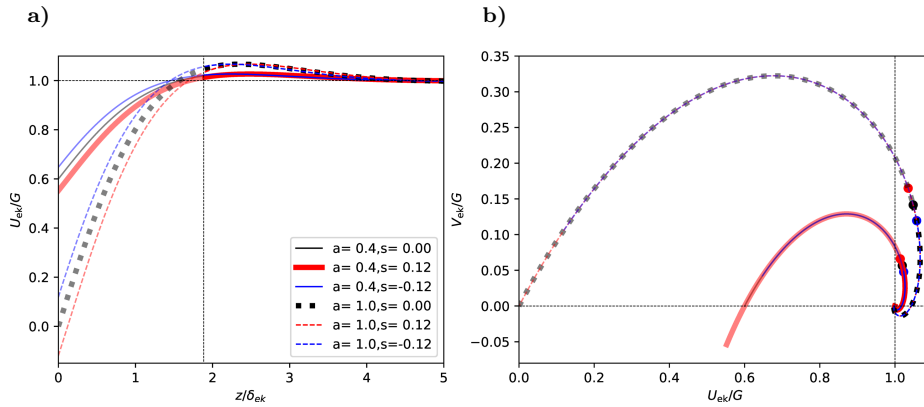


Fig. 5 a) Generalized Ekman-profile of the geostrophic-aligned component U_{ek} . b) Hodograph for the geostrophic-aligned and pressure-gradient aligned components U_{ek} and V_{ek} . Thick, black dashed line shows the classic solution. The height corresponding to $z^- = 0.30$ is marked by the dashed line in panel (a) and by filled circles in panel (b). The hodograph and profiles above this reference height are shown as solid lines, below as opaque line.

415 visual comparison, and we find $a_{ek} = 8.4u_*$; while this appears rather large, it is
 416 pre-multiplied by $e^{-z_{ek}}$ which has already decreased to $\mathcal{O}(0.1)$ at the height of this
 417 maximum. This choice ascertains that the velocity deficits $U/u_* - Z_*$ and $V/u_* - Z_*$
 418 do not depend on the velocity scale u_* , but only on G as

$$U_{ek}/u_* - Z_* \propto a_{ek}Z_* = 8.4G. \quad (11)$$

419 **The offset parameter** s_{ek} defines the zero-crossing height of the profile (in
 420 contrast to δ_{ek} , which determines the thickness across which the wind veering
 421 takes place). Physically, this offset can be understood as the height at which the
 422 surface was located assuming a perfect Ekman flow down to the surface. As this
 423 is not the case, and gradients are steeper in the highly turbulent boundary layer
 424 flow encountered when approaching the surface, the offset is smaller than zero (the
 425 fully turbulent boundary layer is actually thinner than an Ekman layer would be).
 426 From our DNS data, we estimate $s_{ek} = -0.12$.

427 In summary, the outer layer of Ekman flow is characterized by a turning of
 428 the wind velocity and the super-geostrophic maximum that is sustained by mo-
 429 mentum convergence at the inflection point of the velocity profile. The super-
 430 geostrophic maximum of streamwise velocity and a secondary minimum aloft the
 431 bulk-turbulent part of the boundary layer are well-described by a classic Ekman
 432 spiral with adapted boundary conditions and a shift in reference height. While al-
 433 ternative approaches exist that incorporate a variation of the eddy viscosity (Basu
 434 and Holtslag 2023), we stick here to Ekman's classic assumption of constant eddy
 435 viscosity. As the Ekman spiral is applied only for $z > z_{blend} \approx 0.28$ (cf. Sec. 4.5
 436 below), the assumption of constant eddy viscosity is also weakened in the sense
 437 that it is only required for $z > z_{blend}$. Corresponding profiles are shown in compar-
 438 ision with data from three DNS runs in Fig. 6. The idealized profiles capture the
 439 secondary minimum and convergence to the geostrophic equilibrium in the non-
 440 turbulent flow very well. Deviations from the Ekman spiral are found towards the
 441 lower end of the corresponding height range, marked by a dot in the figure; this is

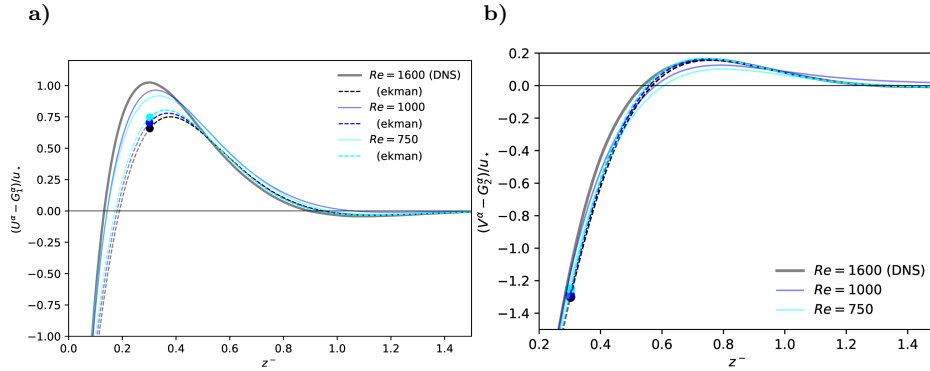


Fig. 6 Shear-aligned velocity deficit for the streamwise (panel **(a)**) and spanwise (panel **(b)**) components of the mean velocity U^α and V^α . Solid lines show DNS data, dashed lines the Ekman profiles U_{ek} and V_{ek} as defined in Eq. 10. Variations in U_{ek} and V_{ek} are a consequence of the normalization and related to changes in u_* and α_* among the different Re_D .

442 consistent with an increasing variation of eddy viscosity when the more turbulent
443 part of the boundary layer is entered from aloft.

444 4.3 Streamwise velocity component

445 Well-established theories exist for the streamwise velocity profile, which in non-
446 rotating flows is aligned with the surface shear stress due to the geometry. These
447 theories cover various regimes based on their distance from the wall and the relative
448 influence of viscosity, turbulence, and interaction with the outer flow region, with
449 the logarithmic law for the mean velocity serving as a central reference point.

450 In immediate vicinity to the surface, local turbulent mixing cannot occur for
451 the no-slip/no-penetration boundary condition, and the mean velocity is described
452 by a viscous profile of the form

$$U^{\alpha_*+} = z^+ \quad (12a)$$

453 where the direction of the velocity points into the exact opposite direction of the
454 wall shear stress τ . In absence of roughness elements and for small roughness
455 ($z_0^+ < 5$), this linear regime is known as viscous sub-layer Foken (2002); Foken
456 et al. (1978). In fact, this law of the wall has no degree of freedom given the
457 drag, i.e. once u_* and α_* are defined. However, theoretical foundation is lacking
458 for the exact shape of the velocity profile in the buffer layer; though crucial for
459 turbulence production, it is commonly understood as a transition region between
460 the linear profile at the surface and the logarithmic profile aloft. A pure blending
461 from the linear velocity profile into the logarithmic one is, however, not reasonable
462 as both the linear and logarithmic profile overestimate the velocity in the buffer
463 layer. We therefore introduce a two-step correction procedure, accounting for the
464 smaller-than linear growth beyond $z^+ \approx 5$, and assuring smooth matching with

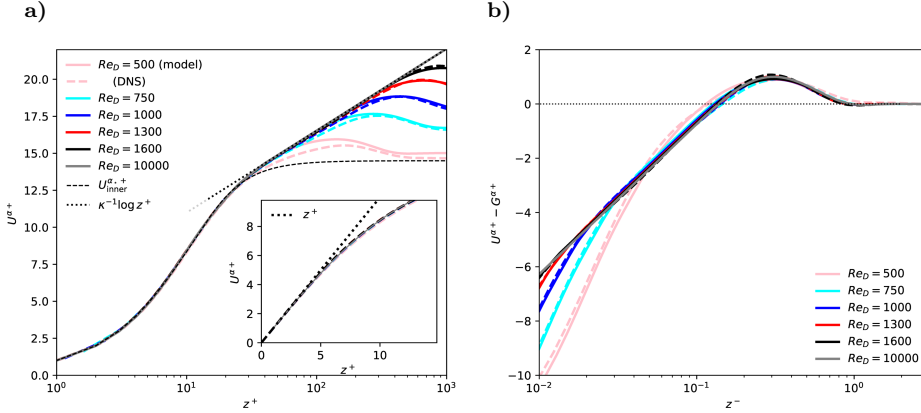


Fig. 7 Shear-aligned profiles of velocity components $U^{\alpha*+}$ in inner (left) and outer (right) units.

465 the logarithmic law at $z^+ = 40$:

$$U_{\text{inner}}^{\alpha*+} = \frac{z^+}{1 + c_1(y^+)^2} + (c_2 z^+ - a_{\text{match}}) \frac{1 + \tanh[0.2(z^+ - 22)]}{2} + c_3 e^{-c_4(z^+ - 22)^2}. \quad (12b)$$

466 We use here

$$c_1 = 0.00185; \quad c_2 = 0.195; \quad c_3 = 0.4; \quad c_4 = 0.35.$$

467 The second and third terms on the right hand side vanish for $z^+ \ll 22$, and
468 $c_1 = 0.00185$ implies an approximately 5% correction at $z^+ = 5$ and an 18.5%
469 correction at $z^+ = 10$. The second and third term on the R.H.S. of eq. (12b) are
470 an empirical fit to the velocity profiles observed in the buffer layer and appear
471 independent of the Reynolds number for the range observed here. The coefficient
472 a_{match} , which has no effect in the viscous sublayer, is then used to match this
473 formulation to the logarithmic law employed above.

474 In the logarithmic region, we use the profile

$$U_{\log}^{\alpha*+} = \frac{1}{\kappa} \log z^+ + C \quad (12c)$$

475 with the von-Kármán constant $\kappa = 0.416$ and the boundary condition $C = 5.4605$.

476 For this logarithmic law, $a_{\text{match}} = 3.569861$ for a matching at $z^+ = 40$.

477 4.4 Spanwise velocity component

478 The background rotation and associated veering of the surface wind implies a
479 non-zero profile for the span-wise velocity which challenges the conventional as-
480 sumptions related to the channel-flow analogy: While the analogy with channel
481 flow in vicinity of the wall implies that the streamwise component be zero or at
482 least small, the veering requires a value of $V_{top} = U_G \sin \alpha_*$ in the free stream (and
483 thus also at the top of the boundary layer if we assume that any substantial veloc-
484 ity gradient is confined to the turbulent part of the flow). This continuous rotation

485 of the wind vector is conveniently visualized by velocity hodographs aligned with
 486 the outer, geostrophic flow (cf. Fig. 5b) and normalized by the geostrophic wind.
 487 The geometry of the flow and its drag imply the following for any hodograph: (i)
 488 the boundary conditions at the surface, (ii) the boundary condition at the top,
 489 and (iii) the inclination of the hodograph at the origin by the surface veering:

$$V^{\alpha_*}(z = 0) = 0, \quad (13a)$$

$$\lim_{z \rightarrow \infty} V^{\alpha_*} = G \sin \alpha_* \quad (13b)$$

$$\partial_{z+} V^{\alpha_*+}|_{z=0} = 0. \quad (13c)$$

490 Outer scaling of the velocity profile further implies that the velocity deficit
 491 of $(V^{\alpha_*} - G^{\alpha_*})/u_*$ be a universal function of the outer height z^- . In the outer
 492 region of the flow (for $z^- \mapsto 1$), $f_V(z^-)$, should govern the spanwise velocity
 493 profile, as is supported by our DNS data (Fig. 1b); above $z^- \approx 0.3$, this profile is
 494 very well approximated by the Ekman-turning derived above (Eq. (10); Fig. 6b).
 495 While this deficit is a signature of outer rotation, it is inappropriate to extend this
 496 general relation to the surface where inner scales matter: On the one hand, the
 497 variation of the spanwise velocity deficit across the boundary layer (i.e. between
 498 $0 < z^- < 1$) must match the difference implied by the drag law (u_*, α_*) and the
 499 constant value of V^{α_*} around $z^- = 0.3$. On the other hand, provided the outer
 500 velocity deficit is Re independent—the Re-dependence of α_* and u_* implies that
 501 this difference cannot be constant as a function of Re. We hence ask, how does the
 502 span-wise component scale when the surface is approached? Clearly, the spanwise
 503 contribution is small in comparison with the streamwise component throughout
 504 much of the layer below $z^- \approx 0.3$. However, we cannot assume $V = 0$ if a smooth
 505 matching between the inner and outer layers shall be achieved. In this context, we
 506 first realize that the velocity deficit $(V^{\alpha_*} - G^{\alpha_*})/u_*$ approaches a Re-independent
 507 constant around $C_{V0} = Z_* \sin \alpha = 6.1$ at the surface; deviations from this constant
 508 are only found for the lowest Reynolds numbers which is in accordance with the
 509 low-Re correction suggested by Spalart (1989). This constrains the wind veer, and
 510 it quantitatively shows that the decreasing wall friction manifest in an increase of
 511 Z_* exactly compensates the decrease of wind turning measured by $\sin \alpha_*$.

512 If the difference across the boundary layer is constant (C_{V0}) vs. Re, the av-
 513 eraged gradient $\partial_{z+} V^{\alpha_*+}$ of the spanwise velocity component must decrease as
 514 $1/\delta^+$ with increasing Re_τ . Hence, it should—at a fixed height—be $V^{\alpha_*} \propto (\delta^+)^{-1}$. A
 515 profile that agrees with the constraints of the profile at the surface and exploits
 516 the dependence of V^{α_*} on δ^+ is

$$V^{\alpha_*} \frac{\delta^+}{G} = f_{V,\text{visc}}(z^+) = v_{\text{ref}} (\omega_v z^+ - 1 + \exp[-\omega_v z^+]), \quad (14)$$

517 where v_{ref} controls the magnitude of the profile and ω_v sets the height at which the
 518 profile transitions into an approximately linear one. We find excellent agreement
 519 with the DNS data for $500 \leq Re_D \leq 1600$ below $z^+ \approx 15$ with

$$v_{\text{ref}} = 18.85; \quad \omega_v = 0.2353$$

520 (cf. Fig. 8b).

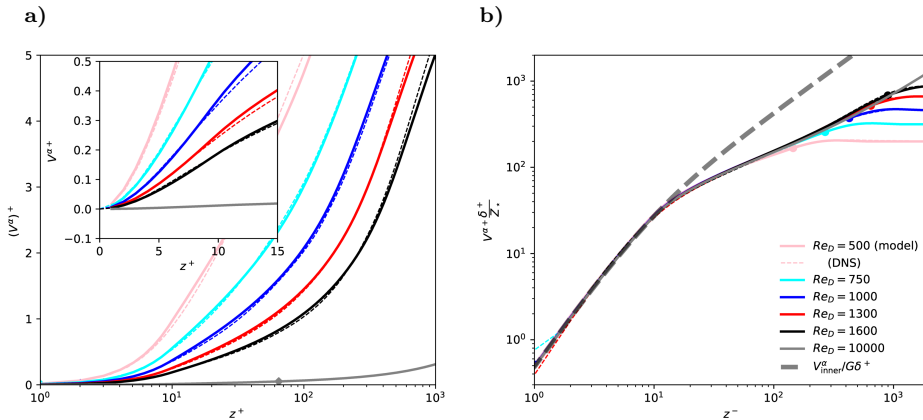


Fig. 8 Profiles of shear-aligned span-wise velocity $(V^\alpha)^+$ versus inner height. Dashed lines show DNS data, thick, opaque lines are from the semi-empirical theory developed above. Panel (a) shows standard inner normalization, panel (b) the inviscid normalization yielding a universal profile for the spanwise component of velocity in the inner layer.

521 For the adjacent surface layer, we find a log-like transition from the quasi-linear
 522 profile inner profile around $z^+ = 10$ to a linear profile with increasing Re (Fig. 8b).
 523 We model this transition by

$$f_{V,\log}(z^+) = \frac{V_{\log}(z^+)}{G} \delta^+ = a_{\log} + b_{\log} \log z^+ + c_{\log} z^+. \quad (15)$$

524 This surface-layer profile matches the inner (viscous) scaling in vicinity of the
 525 surface to the outer (Ekman) scaling above $z^- = 0.3$ when constrained by the
 526 viscous profile at the bottom and the Ekman profile at the top:

$$f_{V,\log}(z^+ = 10) = f_{V,\text{visc}}(z^+ = 10) =: v_{10} \simeq 27.3 \quad (16a)$$

$$\frac{\partial}{\partial z^+} [f_{V,\log}]_{z^+ = 10} = \frac{\partial}{\partial z^+} [f_{V,\text{visc}}]_{z^+ = 10} =: d_{10} \simeq 4.01 \quad (16b)$$

$$f_{V,\log}(z^+ = 0.3\delta^+) = V_{\text{ek}}^{\alpha*}(z^- = 0.3)\delta^+ =: v_{03} \quad (16c)$$

527 where v_{03} is determined by $V_{\text{ek}}(0.3)$ and $U_{\text{ek}}(0.3)$ and depends on Re . Given the
 528 Ekman formulation of the velocity profile introduced in Sec. 4.2, one may express
 529 v_{03} using the Ekman profile introduced in Sec. 4.2 together with the approximation
 530 for $u_*(Re)$ found in Eq. (9). While the Re -dependency of a_{\log} , b_{\log} , c_{\log} is small,
 531 it shows up in Fig. 1 where the normalized profiles of spanwise velocity become
 532 more convex with increasing Re . We can now quantify this effect by means of the
 533 change of c_{\log} versus Re which is shown in Fig. 9 (cf. Appendix A.2; a_{\log} and b_{\log}
 534 are then determined by the universal values of v_{10} and d_{10}).

535 4.5 Matching of the inner and outer layer profiles

536 The formulations introduced above are continuous across the transition from the
 537 inner to the outer layer. However, the requirement of smooth derivatives would
 538 over-constrain the velocity profiles and is hence not applied. This can, in particular

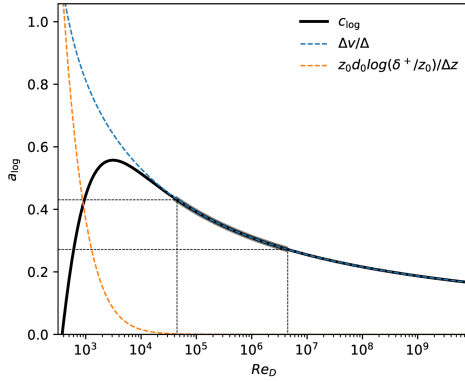


Fig. 9 Coefficients a_{\log} , b_{\log} and c_{\log} (cf. Eq. 15) as a function of the viscous Reynolds number Re_D . The approximate range of scale separation relevant for atmospheric application is found in between the dotted lines, where $a_{\log} \simeq 0$ and $c_{\log} \simeq 0.4$

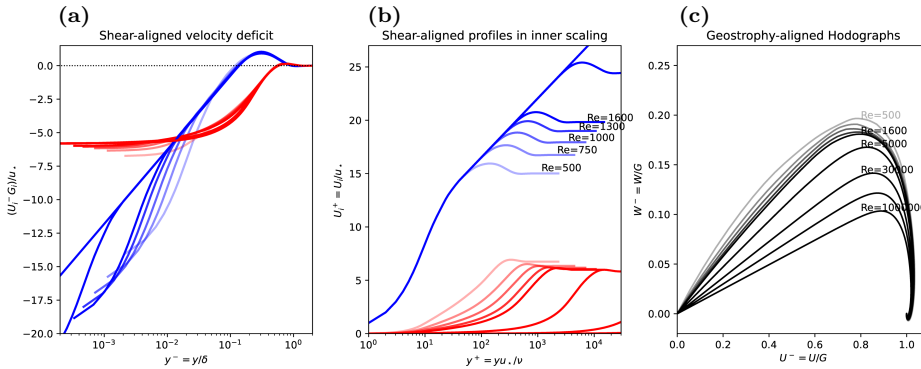


Fig. 10 (a) Velocity deficit, (b) velocity profile in shear-aligned hodographs and (c) hodograph in geostrophy-aligned coordinates. In panels (a) and (b), blue lines correspond to the streamwise component and red to the spanwise.

539 for low or extremely high Re , cause discontinuity in the derivatives of the velocity
 540 profiles around the transition from the inner to the outer layer. To avoid such
 541 artificial discontinuity, the profiles are blended by an error-function transition
 542 using a blending height $z_{blend}^- = 0.28 - 2.25\sqrt{1/Re_\tau}$ and a transition thickness
 543 $z_{trans} = 2$, such that the weighting function $\omega(z^-)$ becomes

$$\omega(z^-) = \frac{1}{2} \left[\operatorname{erf} \left(z_{trans} \log \frac{z^-}{z_{blend}} \right) + 1 \right], \quad (17)$$

544 hence $u_{\text{total}} = (1 - \omega) \times u_{\text{inner}} + \omega \times u_{\text{outer}}$ and similar for v .

545 The resulting velocity profiles across the entire boundary layer are shown in
 546 inner and outer scaling as well as in hodograph-view in Fig. 10. The shear-aligned
 547 velocity deficit is shown in outer scaling highlighting the universality in the outer
 548 layer. The logarithmic scaling of the streamwise component is encountered as
 549 straight blue lines in panels (a) and (b) where the extent of the logarithmic range
 550 increases with Re towards lower values of z^- and higher values of z^+ depending
 551 on the scaling. Importantly, the logarithmic region is widening for increasing

552 Reynolds number – irrespective of the scaling. In this simple inner scaling, the
 553 spanwise velocity (which follows a mixed scaling) does not collapse but seems to
 554 depend on Re (the collapse is seen in Fig. 8). However, the velocity deficit in outer
 555 units becomes approximately universal, also across the inner layer; this reflects
 556 the compensation of reduced turning (α) by increased drag (u_*), and is consistent
 557 with the theoretical considerations discussed in 4.1.

558 The spanwise velocity at a fixed height scales approximately as Re_τ^{-1} (Sec. 4.4).
 559 However, the fraction of turning that is encountered within the inner layer of the
 560 flow amounts to about 1/3 of the total wind veer (Fig. 12a). This is because, in
 561 inner units, the inner layer grows as Re_τ which exactly compensates the reduced
 562 gradient of spanwise velocity. The hodographs show the well-known Ekman shape
 563 with the laminar profile as an outer limit and 'flatter' hodographs, corresponding
 564 to less turning, for increasing Reynolds number.

565 5 Discussion

566 5.1 Implications for surface-layer scaling

567 Eq. (14) establishes a mixed scaling for the spanwise velocity in the viscous layer:
 568 While it requires the vertical coordinate to be expressed in inner units, the velocity
 569 itself is normalized by the geostrophic wind, and becomes inversely proportional
 570 to the friction Reynolds number $Re_\tau = \delta^+$ when considered at a fixed height. In
 571 vicinity of the surface, such mixed scaling has already been identified for higher-
 572 order statistics in convective flows (Mellado et al. 2016; Li et al. 2018), where large
 573 scales leave their signatures in vicinity of the surface. It is important to note here
 574 that, while V is a first-order statistic from a statistical perspective, the spanwise
 575 velocity is a higher-order correction term from the perspective of similarity theory
 576 and from the viewpoint of the channel-flow analogy that is routinely employed
 577 in the surface layer. Further, this is consistent with the scaling for the velocity
 578 hodograph found in Eq. (11) where the friction velocity also drops out.

579 In the surface layer, there is not only a mixed scaling—as we had already iden-
 580 tified in the viscous layer—, but we cannot find a universal function onto which the
 581 profiles of spanwise velocity collapse. This additional degree of freedom reflects
 582 the inner–outer matching problem for the spanwise velocity. Rather than giving a
 583 profile for this region, we resort here to a parametric description of the problem
 584 in terms of the function $f_{V,\log}$ determined by the parameters a_{\log} , b_{\log} , c_{\log} which
 585 can be estimated based on the above scaling considerations for any Reynolds num-
 586 ber. We note that, once the parameter a_{\log} is known, the parameters b_{\log} and c_{\log}
 587 can be estimated solely based on $f_{V,\text{visc}}$, i.e. using the value v_{10} and d_{10} found
 588 for the viscous region of the flow. For the range of Reynolds number relevant to
 589 geophysical problems ($10^4 \lesssim Re_D \lesssim 10^6$), the variation of c_{\log} is, however, rather
 590 small.

591 5.2 Comparison with other theories

592 An alternative approach that considers viscous effects close to the surface is the
 593 van-Driest scaling (Van Driest 1956), where an exponential damping of Prandtl's

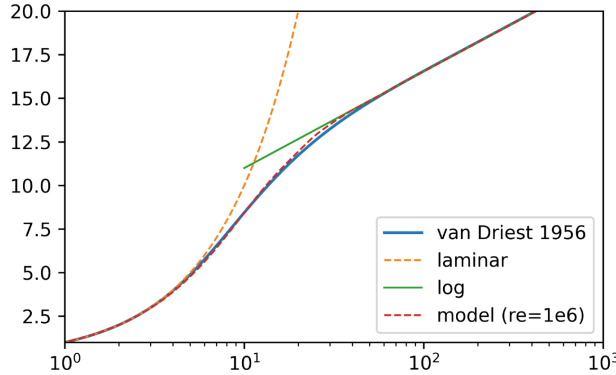


Fig. 11 Near-wall velocity profile according to the van-Driest scaling (blue, solid) in comparison with the present model (red, dashed), the viscous law of the wall (orange dashed), and the logarithmic law (green, solid)

mixing length is considered near the wall to yield

$$\frac{\partial u^+}{\partial z^+} = \frac{2}{1 + \sqrt{1 + (2\kappa z^+)^2 (1 - \exp[-z^+])}}; \quad (18)$$

the spanwise component is zero as no rotational effects are considered. Comparing our proposed formulation for the stream-wise velocity in the inner layer to Van Driest's formulation yields later convergence of the velocity onto the logarithmic profile while, over all, it serves as an excellent model of the streamwise velocity component (Fig. 11): Notable deviations (on the order of few percent) only occur in the region $10 < z^+ < 30$, where the velocity transitions from the linear to the logarithmic profile.

For the higher layers of the ABL, the Ekman spiral is the simplest model available. When employed across the entirety of the ABL, the spiral of a turbulent Ekman layer is flattened with respect to Ekman's laminar solution, which corresponds to a reduction of the veering angle both at the surface and throughout the ABL. We, however, find that a modified version of the Ekman spiral explicitly taking into account the surface boundary condition, is a consistent model and yields excellent agreement with the velocity profiles from DNS (Sec. 4.2).

A two-layer model consolidating both the logarithmic and Ekman layer can be obtained following the arguments by Etling (2008), cf. Emeis (2018). Given a surface veering and a matching height (extent of the logarithmic layer), a formulation for the velocity profile across both the logarithmic and the outer layer is obtained. A comparison using the surface veering based on our model and a matching height of $z_{\text{prandtl}} = 0.05\delta$, which gives better results than the matching height of 0.1δ suggested by Etling (2008), is shown in Fig. 12. The overall shape of velocity magnitude is matched apart from the viscous and buffer layer (cf. Fig. 12b) that is neglected by the two-layer model. However, quantitative departures on the order of 10% occur across the inner layer: it turns out that the non-rotating profile, of the two-layer model in the logarithmic region yields too low overall velocity as the spanwise component contributes to the velocity across the inner layer. Deviations also occur with respect to wind direction; despite the

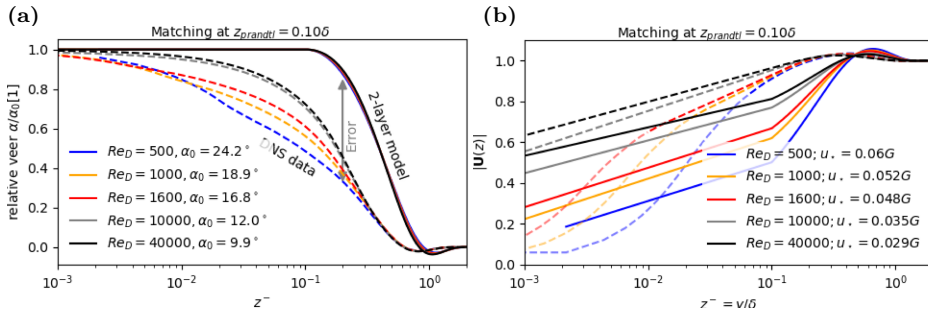


Fig. 12 Comparison of the DNS data (dashed lines) with the two-layer model proposed by Eting (solid lines) for different Reynolds number. Left panel shows the relative wind veer, right panel shows the velocity magnitude. The Eting model is calibrated by the surface veer from the DNS and the roughness parameter is chosen according to the correction factor $\exp \kappa A$ such that the total veer and velocity magnitude agree. Profiles in the buffer layer, defined here as $z^+ < 30$ are shown as opaque dashed lines as the two-layer model does not consider viscous effects.

622 rather low matching height, a substantial fraction of the rotation occurs within
 623 the lower part of the ABL and about 20% of the wind veer is not captured by the
 624 two-layer model. As the overall veer is given, the non-captured veer close to the
 625 surface is then compensated across the logarithmic layer. In the upper part of the
 626 boundary layer, both profiles match well.

627 The interpretation of flux and gradient profiles in terms of the K-theory (cf.
 628 Sec. 3, Fig. 2) suggests a certain universality in the inner layer, while a global
 629 collapse, i.e. across the boundary layer, is not obtained. While the K-Profiles con-
 630 cern the total stress, a consistent formulation of the turning would also require its
 631 partitioning to the individual components, i.e. the orientation of the stress vector
 632 ($u'w'$, $v'w'$) in the horizontal plane. If K-theory shall be used, this stress vector
 633 needs to be anti-parallel to the corresponding stress vector ($\partial_z U$, $\partial_z V$). Fig. 13
 634 shows the direction of the velocity, gradient and stress vectors across the bound-
 635 ary layer. It turns out that the negative stress vector with respect to the wind
 636 direction and the flux vectors (absolute) have an approximately similar direction.
 637 It appears that both rotate by about 270° ($3\pi/2$) across the boundary layer. Apart
 638 from the lower part of the Ekman layer ($0.2 < z^- < 0.7$), where there is a slight
 639 dependence on Re , the direction of stress appears to be universal, which is a
 640 consequence of the Ekman profile introduced in Sec. 4.2. However, this implies
 641 a misalignment between the flux and the stress on the order of the wind turn-
 642 ing, and indeed Fig. 13b shows a misalignment up to $\pi/8$. This is in accordance
 643 with the expectation by (Townsend 1976, Chap. 7.18) and prevents the transfer
 644 of energy from the mean flow to turbulence at these heights, thus preventing a
 645 boundary-layer growth. While the behavior in the inner layer seems to depend on
 646 Re , there emerges universality in the misalignment across the outer layer, suggest-
 647 ing that a consideration of misalignment in the context of K-theory is possible
 648 when developing formulations for higher-order quantities.

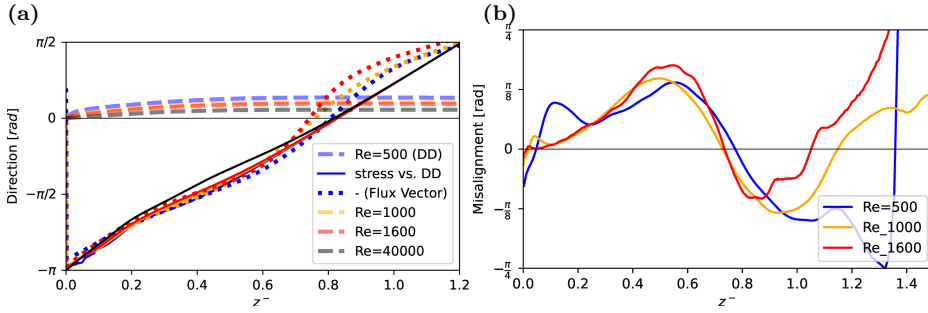


Fig. 13 Panel (a) shows the wind direction (DD) as thick dashed lines and the direction of stress relative to DD as thin solid lines, both according to our profile model. The direction of the negative flux vector ($\bar{u}'w'$, $\bar{v}'w'$) based on DNS data is shown as a dotted line. In panel (b), we plot the misalignment, i.e. the angle, between the flux vector and the shear vector, where the shear vector is defined accordingly as $(\partial_z U, \partial_z V)$.

6 Conclusions

We investigate the wind veer and fundamental scaling properties of the velocity profiles in Ekman flow. Based on scaling considerations and direct numerical simulation spanning a decade in external separation from $Re_A = 1.25 \times 10^5$ to $Re_A = 1.28 \times 10^6$, we derive a closed formulation for both horizontal components of the velocity profile in a stationary, smooth Ekman layer. This formulation is consistent with the DNS data and also yields reasonable results at geophysical scale separation; the logarithmic law of the mean velocity is recovered with the well-known limits and deviations towards the surface and Ekman layer. The classic formulation of the Ekman layer, employing the surface boundary condition, is replaced by a modified solution that can be obtained by Ekman's system of governing equations, but using different boundary conditions that are more appropriate of the actual situation encountered in the planetary boundary layer. The three parameters that characterize this boundary condition are estimated based on DNS data.

To quantify the spanwise velocity component consistently across the boundary layer, we derive a universal scaling of the spanwise velocity component in a shear-aligned reference frame. For the *inner layer*, we find the mixed scaling

$$V^{\alpha_*}/G = \frac{1}{\delta^+} f(z^+) \quad (19)$$

that is, the spanwise velocity normalized by the outer velocity scale is a universal function of the inner height and Friction Reynolds number $Re_\tau = \delta^+$. This scaling is derived here based on scaling considerations, and it is in excellent agreement with the DNS data available. In the outer layer, the spanwise velocity follows outer scaling, consistently with the Ekman model discussed above (Sec. 4.2).

Our results suggest that there is no lower limit of the turning. Hence—despite its very large scale separation / huge Reynolds number—the ABL is not in the ‘limit’ of high Reynolds number from the perspective of wind veer, but always in a regime where changes in Re impact on the vertical partitioning of rotation.

676 A Appendices
677 A.1 Laminar Ekman solution with consideration of inner layer

678 The following Ekman system is obtained by averaging the Navier–Stokes equations horizontally
 679 and over time and neglecting the turbulent transport terms (turbulence can then be considered
 680 via variation of the vertically constant eddy viscosity ν ; for a height-dependent eddy-viscosity
 681 model, the reader is referred to Basu and Holtslag (2023)):

$$\left(\frac{\partial_t U}{\partial_t V} \right) = \left(\begin{array}{c} fV \\ -f(U-G) + \nu \partial_z^2 V \end{array} \right) \quad (20a)$$

$$\Rightarrow \partial_t(U+iV) = f(V-i(U-G)) + \nu \partial_z^2(U+iV) \quad (20b)$$

682 In stationary conditions, this system is solved by

$$\hat{u}(z) = U_\infty + e^{-\gamma z} [A \cos \gamma z + B \sin \gamma z] \quad (20c)$$

$$\hat{v}(z) = V_\infty + e^{-\gamma z} [-A \sin \gamma z + B \cos \gamma z] \quad (20d)$$

683 where the constants U_∞ , V_∞ set the top boundary condition and A and B set the bottom
 684 boundary condition. The most common boundary condition for a surface Ekman layer is $A =$
 685 $U_\infty = G$, $B = 0$, and $V_\infty = 0$. The lower boundary condition, however, neglects the existence
 686 of the surface layer, and it appears reasonable to define $A = cG$ where $c < 1$ is a constant that
 687 incorporates the increased shear in the surface layer. Given a ‘matching height’ z_{match} and
 688 normalized matching height $\xi = \gamma z_{\text{match}}$ in the upper part of the inner layer, we can match
 689 the Ekman profile to the inner layer by letting

$$\begin{aligned} u(z_{\text{match}}) &\equiv u_{\text{match}} = U_\infty + e^{-\xi} [A \cos \xi + B \sin \xi] \\ v(z_{\text{match}}) &\equiv v_{\text{match}} = V_\infty + e^{-\xi} [-A \sin \xi + B \cos \xi] \end{aligned} \quad (21a)$$

$$\Rightarrow \begin{pmatrix} u_{\text{match}} - U_\infty \\ v_{\text{match}} - V_\infty \end{pmatrix} = e^{-\xi} \begin{pmatrix} A \\ B \end{pmatrix} \begin{pmatrix} \cos \xi & +\sin \xi \\ -\sin \xi & +\cos \xi \end{pmatrix} \quad (21b)$$

$$(21c)$$

690 Matching the profile at $\xi = 0$, one obtains $A = \Delta u_{\text{match}}$ and $B = -\Delta v_{\text{match}}$; and when the
 691 direction Ox is aligned with the geostrophic wind, we obtain the textbook-case $A = |\mathbf{G}|$ and
 692 $B = 0$.

693 Otherwise, choosing $B \neq 0$ allows to introduce a phase shift of the Ekman rotation with
 694 respect to the decay of the wind spiral. However, in our context, the thickness and position of
 695 the spiral can already be controlled by the eddy viscosity and an offset in ξ , here we let $B = 0$.

697 A.2 Matching the spanwise velocity profiles in the inner layer

698 The spanwise profile in vicinity of the surface is given by $V/G = f_{V,\text{visc}} \delta^+$ with

$$f_{V,\text{visc}} = v_{\text{ref}} (\omega_v z^+ - 1 + e^{-\omega_v z^+}) \quad (22a)$$

$$f_{V,\log} = a_{\log} + b_{\log} \log z^+ + c_{\log} z^+ \quad (22b)$$

699 Matching the profiles and gradient $z_0^+ = 10$ and the value at $z_1 = 0.3\delta^+$ yields

$$v_{\text{ref}} (\omega_v z_0 + e^{-\omega_v z_0}) = v_0 = a_{\log} + b_{\log} \log z_0 + c_{\log} z_0 \quad (23a)$$

$$v_1 = a_{\log} + b_{\log} \log z_1 + c_{\log} z_1 \quad (23b)$$

$$v_{\text{ref}} \omega_z (1 - e^{-\omega_z z_0}) = d_0 = \frac{b_{\log}}{z_{10}} + c_{\log} \quad (23c)$$

700 The gradient condition implies $b_{\log} = (d_0 - c_{\log})z_0$, and yields

$$v_0 - z_0 d_0 \log z_0 = a_{\log} + c_{\log}(z_0 - z_0 \log z_0) \quad (24a)$$

$$v_1 - z_0 d_0 \log z_1 = a_{\log} + c_{\log}(z_1 - z_0 \log z_0) \quad (24b)$$

$$\Rightarrow c_{\log} = \frac{\Delta v - z_0 d_0 \log z_1 / z_0}{\Delta z} \quad (24c)$$

701 with $\Delta z = z_1 - z_0$ and $\Delta v = v_1 - v_0$. Then, the coefficient a_{\log} is estimated as

$$a_{\log} = v_0 - z_0 d_0 \log z_0 - \frac{\Delta v - z_0 d_0 \log z_1 / z_0}{\Delta z} [z_0 - z_0 \log z_0]. \quad (24d)$$

702 We note that $\log(z_1/z_0)/(z_1 - z_0) \rightarrow 0$ for large z_1 , and as $z_1 = 0.3\delta^+$, this implies that the
703 second term in c_{\log} only plays a role at low and intermediate Re. Then, a_{\log} can be estimated
704 as

$$a_{\log} \simeq v_0 - z_0 \left[d_0 \log z_0 - \frac{\Delta v}{\Delta z} (1 - \log z_0) \right] \quad (24e)$$

705 for large Re.

706 **Acknowledgements** We thank Sukanta Basu and two anonymous reviewers for their valuable
707 reviews of this manuscript. Simulations were carried out on the German supercomputing
708 systems **hawk** at HÖCSTLEISTUNGSRECHENZENTRUM STUTTGART (Bundesprojekt 44187) and **juwels** at
709 GAUSS CENTRE FOR SUPERCOMPUTING, FORSCHUNGZENTRUM JÜLICH (Projects **hku24** and **stadit**). We
710 extend our thanks to Sally Issa for valuable feedback on the manuscript.

711 Declarations

712 **Author contributions** CA conceived the study, acquired funding, performed the simulation,
713 analysed and plotted the data for this work. CA and HW interpreted the data and compiled
714 the manuscript.

715 **Funding** CA is funded by the European Commission's 7th Framework Programme through
716 the ERC 2019 Starting Grant trainABL (ID 851374). HW is funded by the Ministry for Science
717 and Culture of Lower Saxony (project *ZukunftsKonzept Windenergieforschung*). Open Access
718 funding for this publication through the DEAL agreement.

719 **Data availability** The data is available in long-term repositories and indexed by DOIs as
720 cited in the list of references. Further analysis tools and processed data can be made available
721 upon direct request.

722 **Conflict of interest** The Authors declare no competing interest.

723 **Open access** This article is licensed under a Creative Commons Attribution 4.0 International
724 License, which permits use, sharing, adaptation, distribution and reproduction in any medium
725 or format, as long as you give appropriate credit to the original author(s) and the source,
726 provide a link to the Creative Commons licence, and indicate if changes were made. To view
727 a copy of this licence, visit <https://creativecommons.org/licenses/by/4.0/>.

728 References

- 729 Ansorge C (2019) Scale Dependence of Atmosphere–Surface Coupling Through Similarity Theory. Boundary-Layer Meteorol 170(1):1–27, DOI 10.1007/s10546-018-0386-y
730
731 Ansorge C (2024a) Direct numerical simulation of turbulent Ekman flow (Re=0500): DOI
732 10.17169/refubium-42505. DOI 10.17169/refubium-42505
733 Ansorge C (2024b) Direct numerical simulation of turbulent Ekman flow (Re=1000): DOI
734 10.17169/refubium-42507. DOI 10.17169/refubium-42507

- Ansorge C (2024c) Direct numerical simulation of turbulent Ekman flow ($Re=1300$): DOI 10.17169/refubium-42508. DOI 10.17169/refubium-42508
- Ansorge C (2024d) Direct numerical simulation of turbulent Ekman flow ($Re=1600$): DOI 10.17169/refubium-42509. DOI 10.17169/refubium-42509
- Ansorge C, Mellado JP (2014) Global Intermittency and Collapsing Turbulence in the Stratified Planetary Boundary Layer. *Boundary-Layer Meteorol* 153(1):89–116, DOI 10.1007/s10546-014-9941-3
- Ansorge C, Mellado JP (2016) Analyses of external and global intermittency in the logarithmic layer of Ekman flow. *J Fluid Mech* 805:611–635, DOI 10.1017/jfm.2016.534
- Baars WJ, Marusic I (2020) Data-driven decomposition of the streamwise turbulence kinetic energy in boundary layers. Part 2. Integrated energy and. *J Fluid Mech* 882:A26, DOI 10.1017/jfm.2019.835
- Barenblatt GI (1993) Scaling laws for fully developed turbulent shear flows. Part 1. Basic hypotheses and analysis. *J Fluid Mech* 248:513–520, DOI 10.1017/S0022112093000874
- Barenblatt GI, Goldenfeld N (1995) Does fully developed turbulence exist? Reynolds number independence versus asymptotic covariance. *Phys Fluids* 7(12):3078–3082, DOI 10/bw2sq5
- Basu S, Holtslag AAM (2023) A novel approach for deriving the stable boundary layer height and eddy viscosity concepts from the Ekman equations. *Boundary-Layer Meteorol* (187):105–115, DOI 10.1007/s10546-023-00974-x
- Blackadar AK, Tennekes H (1968) Asymptotic Similarity in Neutral Barotropic Planetary Boundary Layers. *Journal of the Atmospheric Sciences* 25:1015–1020, DOI 10.1175/1520-0469(1968)025<1015:ASINBP>2.0.CO;2
- Brown AR, Beljaars ACM, Hersbach H, Hollingsworth A, Miller M, Vasiljevic D (2005) Wind turning across the marine atmospheric boundary layer. *Quarterly Journal of the Royal Meteorological Society* 131(607):1233–1250, DOI 10/dw2bxz
- Calaf M, Meneveau C, Meyers J (2010) Large eddy simulation study of fully developed wind-turbine array boundary layers. *Phys Fluids* 22(1):015,110, DOI 10/b7gc6v
- Coleman GN, Ferziger JH, Spalart PR (1992) Direct Simulation of the Stably Stratified Turbulent Ekman Layer. *Journal of Fluid Mechanics* 244:677–712, DOI 10.1017/S0022112092003264
- da Silva CB, Hunt JC, Eames I, Westerweel J (2014) Interfacial Layers Between Regions of Different Turbulence Intensity. *Annu Rev Fluid Mech* 46(1):567–590, DOI 10.1146/annurev-fluid-010313-141357
- Dimotakis PE (2005) TURBULENT MIXING. *Annual Review of Fluid Mechanics* 37(1):329–356, DOI 10.1146/annurev.fluid.36.050802.122015
- Ekman VW (1905) On the influence of the earth's rotation on ocean currents. *Ark Mat Astron Fys*, Vol 2 (1905), pp 1–53 2:1–53
- Ellison TH (1955) The Ekman spiral. *Q J Roy Met Soc* 81(350):637–638, DOI 10.1002/qj.49708135025
- Emeis S (2018) Wind Energy Meteorology, 2nd edn. *Atmospheric Physics for Wind Power Generation*, Springer, Heidelberg
- Emeis S, Baumann-Stanzer K, Piringer M, Kallistratova M, Kouznetsov R, Yushkov V (2007) Wind and turbulence in the urban boundary layer analysis from acoustic remote sensing data and fit to analytical relations. *metz* 16(4):393–406, DOI 10.1127/0941-2948/2007/0217
- Esau I (2004) Simulation of Ekman Boundary Layers by Large Eddy Model with Dynamic Mixed Subfilter Closure. *Environmental Fluid Mechanics* 4(3):273–303, DOI 10/b8f3kh
- Eting D (2002) Theoretische Meteorologie, 2nd edn. Eine Einführung, Springer-Verlag, Berlin, Heidelberg
- Eting D (2008) Theoretische Meteorologie: eine Einführung, 3rd edn. Springer, Berlin Heidelberg
- Foken T (2002) Some aspects of the viscous sublayer. *metz* 11(4):267–272, DOI 10.1127/0941-2948/2002/0011-0267
- Foken Th, Kitajgorodskij SA, Kuznecov OA (1978) On the dynamics of the molecular temperature boundary layer above the sea. *Boundary-Layer Meteorol* 15(3):289–300, DOI 10.1007/BF02652602
- Ghannam K, Bou-Zeid E (2021) Baroclinicity and directional shear explain departures from the logarithmic wind profile. *Quarterly Journal of the Royal Meteorological Society* 147:434–464, DOI 10/gnj6z2
- Gryning SE, Batchvarova E, Brümmer B, Jørgensen H, Larsen S (2007) On the extension of the wind profile over homogeneous terrain beyond the surface boundary layer. *Boundary-Layer Meteorol* 128(1):1–16, DOI 10.1007/s10546-006-9162-0

- 795 Meteorol 124(2):251–268, DOI 10.1007/s10546-007-9166-9
796 Höglström U (1988) Non-dimensional wind and temperature profiles in the atmospheric surface
797 layer: A re-evaluation. Boundary-Layer Meteorology 42:55–78, DOI 10.1007/BF00119875
798 Höglström U (1996) Review of some basic characteristics of the atmospheric surface layer.
799 Boundary-Layer Meteorology 78(3-4):215–246, DOI 10.1007/BF00120937
800 Jacobs AF, Van Boxel JH (1988) Changes of the displacement height and roughness length
801 of maize during a growing season. Agricultural Forest Meteorol 42(1):53–62, DOI 10.1016/
802 0168-1923(88)90066-4
803 Jiang Q, Wang S, Sullivan P (2018) Large-Eddy Simulation Study of Log Laws in a Neutral
804 Ekman Boundary Layer. Journal of the Atmospheric Sciences 75(6):1873–1889, DOI 10.
805 1175/JAS-D-17-0153.1
806 Jiménez J (2012) Cascades in Wall-Bounded Turbulence. Ann Rev Fluid Mech 44(Volume 44,
807 2012):27–45, DOI 10.1146/annurev-fluid-120710-101039
808 Kelly M, Gryning SE (2010) Long-Term Mean Wind Profiles Based on Similarity Theory.
809 Boundary-Layer Meteorol 136(3):377–390, DOI 10.1007/s10546-010-9509-9
810 Kelly M, Troen I (2016) Probabilistic stability and ‘tall’ wind profiles: Theory and method for
811 use in wind resource assessment. Wind Energy 19(2):227–241, DOI 10.1002/we.1829
812 Klein M, Maier RE, Schmidt H (2021) Stochastic modeling of transient neutral and stably-
813 stratified Ekman boundary layers. P A M M 21(1):e202100,146, DOI 10.1002/pamm.
814 202100146
815 Li Q, Gentine P, Mellado JP, McColl KA (2018) Implications of Nonlocal Transport and
816 Conditionally Averaged Statistics on Monin–Obukhov Similarity Theory and Townsend’s
817 Attached Eddy Hypothesis. J Atmos Sci 75(10):3403–3431, DOI 10.1175/JAS-D-17-0301.1
818 Lindvall J, Svensson G (2019) Wind turning in the atmospheric boundary layer over land. Q
819 J Roy Met Soc 145(724):3074–3088, DOI 10.1002/qj.3605
820 Mellado J, Ansorge C (2012) Factorization of the Fourier transform of the pressure-Poisson
821 equation using finite differences in colocated grids. Z angew Math Mech 92(5):380–392,
822 DOI 10.1002/zamm.201100078
823 Mellado JP, van Heerwaarden CC, Garcia JR (2016) Near-Surface Effects of Free Atmosphere
824 Stratification in Free Convection. Boundary-Layer Meteorol 159(1):69–95, DOI 10.1007/
825 s10546-015-0105-x
826 Mirocha JD, Churchfield MJ, Muñoz-Esparza D, Rai RK, Feng Y, Kosović B, Haupt SE,
827 Brown B, Ennis BL, Draxl C, Sanz Rodrigo J, Shaw WJ, Berg LK, Moriarty PJ, Linn RR,
828 Kotamarthi VR, Balakrishnan R, Cline JW, Robinson MC, Ananthan S (2018) Large-eddy
829 simulation sensitivities to variations of configuration and forcing parameters in canonical
830 boundary-layer flows for wind energy applications. Wind Energy Science 3(2):589–613, DOI
831 10/gn3nh4
832 Moin P, Mahesh K (1998) Direct numerical simulation: A tool in turbulence research. Annual
833 Review of Fluid Mechanics 30:539–578, DOI 10.1146/annurev.fluid.30.1.539
834 Momen M, Bou-Zeid E (2016) Large-Eddy Simulations and Damped-Oscillator Models of the
835 Unsteady Ekman Boundary Layer*. Journal of the Atmospheric Sciences 73(1):25–40, DOI
836 10.1175/JAS-D-15-0038.1
837 Momen M, Bou-Zeid E, Parlange MB, Giometto M (2018) Modulation of Mean Wind and
838 Turbulence in the Atmospheric Boundary Layer by Baroclinicity. Journal of the Atmospheric
839 Sciences 75(11):3797–3821, DOI 10/gfmn67
840 Monin AS (1970) The Atmospheric Boundary Layer. Annual Review of Fluid Mechanics 2:225–
841 250, DOI 10.1146/annurev.fl.02.010170.001301
842 Monin AS, Yaglom AM (1975) Statistical Fluid Mechanics, Vol. II, Dover Publications on
843 Physics, vol II. Dover Publications, Inc., Mineola
844 Optis M, Monahan A, Bosveld FC (2014) Moving Beyond Monin–Obukhov Similarity The-
845 ory in Modelling Wind-Speed Profiles in the Lower Atmospheric Boundary Layer un-
846 der Stable Stratification. Boundary-Layer Meteorology 153(3):497–514, DOI 10.1007/
847 s10546-014-9953-z
848 Rossby CG, Montgomery RB (1935) The layer of frictional influence in wind and ocean cur-
849 rents. Papers in Physical Oceanography and Meteorology III(3):1–101
850 Sakagami Y, Haas R, Passos JC (2020) Generalized Non-dimensional Wind and Temperature
851 Gradients in the Surface Layer. Boundary-Layer Meteorol 175(3):441–451, DOI 10.1007/
852 s10546-020-00510-3
853 Spalart PR (1989) Theoretical and numerical study of a three-dimensional turbulent boundary
854 layer. J Fluid Mech 205(-1):319, DOI 10.1017/S0022112089002053

- 855 Spalart PR, Coleman GN, Johnstone R (2008) Direct numerical simulation of the Ekman layer:
856 A step in Reynolds number, and cautious support for a log law with a shifted origin. *Phys
857 Fluids* 20(10):101,507, DOI 10.1063/1.3005858
- 858 Spalart PR, Coleman GN, Johnstone R (2009) Retraction: “Direct numerical simulation of the
859 Ekman layer: A step in Reynolds number, and cautious support for a log law with a shifted
860 origin” [*Phys. Fluids* 20, 101507 (2008)]. *Phys Fluids* 21(10):109,901, DOI 10.1063/1.3247176
- 861 Stoll R, Gibbs JA, Salesky ST, Anderson W, Calaf M (2020) Large-Eddy Simulation of the At-
862 mospheric Boundary Layer. *Boundary-Layer Meteorol* 177(2-3):541–581, DOI 10/gmbmzw
- 863 Svensson G, Holtslag AAM (2009) Analysis of Model Results for the Turning of the Wind
864 and Related Momentum Fluxes in the Stable Boundary Layer. *Boundary-Layer Meteorol*
865 132(2):261–277, DOI 10/bwknmt
- 866 Tennekes H (1973) A Model for the Dynamics of the Inversion Above a Convective Boundary
867 Layer. *Journal of the Atmospheric Sciences*
- 868 Townsend AA (1976) The Structure of Turbulent Shear Flow, 2nd edn. Cambridge University
869 Press
- 870 Van Driest ER (1956) On Turbulent Flow Near a Wall. *Journal of the Aeronautical Sciences*
871 23(11):1007–1011, DOI 10.2514/8.3713
- 872 Zikanov O, Slinn DN, Dhanak MR (2003) Large-eddy simulations of the wind-induced turbu-
873 lent Ekman layer. *J Fluid Mech* 495:343–368, DOI 10/ccbpbw